Journal of Advanced Ceramics
2024, **13**(2): 155–165
https://doi.org/10.26599/JAC.2024.9220828

Research Article

Ultrahigh *Q* $Sr_{1+x}Y_2O_{4+x}$ (x = 0–0.04) microwave dielectric ceramics for temperature-stable millimeter-wave dielectric resonator antennas

Guoqiang He[1], Yu Jiang[2], Kaixin Song[2,✉], Yanjun Liu[1], Yuan Nie[1], Wenjie Zhang[1], Ziqi Zhao[1], Yinghan He[1], Xinyue Ma[1], Xiuli Chen[1], Xu Li[1,✉], Huanfu Zhou[1,✉]

[1] *Collaborative Innovation Centre for Exploration of Hidden Nonferrous Metal Deposits and Development of New Materials in Guangxi, Key Laboratory of Nonferrous Materials and New Processing Technology, Ministry of Education, School of Materials Science and Engineering, Guilin University of Technology, Guilin 541004, China*
[2] *College of Electronic Information, Hangzhou Dianzi University, Hangzhou 310018, China*

Received: August 30, 2023; Revised: October 25, 2023; Accepted: November 17, 2023

Abstract: Microwave dielectric ceramics should be improved to advance mobile communication technologies further. In this study, we prepared $Sr_{1+x}Y_2O_{4+x}$ (x = 0–0.04) ceramics with nonstoichiometric Sr^{2+} ratios based on our previously reported SrY_2O_4 microwave dielectric ceramic, which has a low dielectric constant and an ultrahigh quality factor (*Q* value). The ceramic exhibited a 33.6% higher *Q*-by-frequency ($Q×f$) value ($Q \approx 12{,}500$) at x = 0.02 than SrY_2O_4. All $Sr_{1+x}Y_2O_{4+x}$ (x = 0–0.04) ceramics exhibited pure phase structures, although variations in crystal-plane spacings were observed. The ceramics are mainly composed of Sr–O, Y1–O, and Y2–O octahedra, with the temperature coefficient of the resonant frequency (τ_f) of the ceramic increasing with Y2–O octahedral distortion. The ceramic comprises uniform grains with a homogeneous elemental distribution, clear grain boundaries, and no obvious cavities at x = 0.02. The $Sr_{1+x}Y_2O_{4+x}$ (x = 0–0.04) ceramics exhibited good microwave dielectric properties, with optimal performance observed at x = 0.02 (dielectric constant (ε_r) = 15.41, $Q×f$ = 112,375 GHz, and τ_f = −17.44 ppm/℃). The τ_f value was reduced to meet the temperature-stability requirements of 5G/6G communication systems by adding $CaTiO_3$, with $Sr_{1.02}Y_2O_{4.02}$+2wt%$CaTiO_3$ exhibiting ε_r = 16.14, $Q×f$ = 51,004 GHz, and τ_f = 0 ppm/℃. A dielectric resonator antenna prepared using $Sr_{1.02}Y_2O_{4.02}$+2wt%$CaTiO_3$ exhibited a central frequency of 26.6 GHz, with a corresponding gain and efficiency of 3.66 dBi and 83.14%, respectively. Consequently, $Sr_{1.02}Y_2O_{4.02}$-based dielectric resonator antennas are suitable for use in 5G millimeter-wave band (24.5–27.5 GHz) applications.

Keywords: millimeter wave; microwave dielectric ceramics; dielectric resonator antenna; nonstoichiometric ratio

1 Introduction

Recent fifth-generation (5G) and sixth-generation (6G) advancements in mobile communication technologies require high-quality data to be transmitted at considerably high rates. Accordingly, the signal-transmission time delay, which is proportional to the square root of the dielectric constant, must be reduced to achieve these outcomes. Consequently, microwave dielectric ceramics, which are essential mobile-technology components with low dielectric constants ($\varepsilon_r < 20$), are required. However, most 5G networks are deployed in the millimeter-wave band, inevitably leading to higher signal attenuation. Moreover, weather factors, such as rain, should be considered. Consequently, filters with larger power capacities are required to improve signal strength and deliver high-quality transmissions over long distances; such filters can be obtained using microwave dielectric ceramics with high quality factors (*Q* values) [1–7]. Accordingly, ultralow dielectric loss ($Q > 5000$) is a basic ceramic requirement. In addition, the temperature coefficient of the resonant frequency (τ_f) is an essential parameter of a microwave dielectric ceramic. As the central frequency of a dielectric resonator typically corresponds to the frequency of a specific resonant mode of the dielectric ceramic, a τ_f value close to zero is required to eliminate temperature drift associated with the resonant frequency [8–14]. Consequently, a low dielectric constant ($\varepsilon_r < 20$), ultralow dielectric loss ($Q > 5000$), and a near-zero τ_f value are currently the top priorities in the microwave dielectric materials.

SrY_2O_4 has been widely used in photoluminescence and thermoluminescence applications, fuel cells, field-emission displays, and thermal barrier coatings. In addition, because doping with various ions (Er^{3+} and Ce^{3+}) results in a variety of colors, SrY_2O_4 has been used as a phosphor [15–21]. Although SrY_2O_4 ceramics exhibit good microwave dielectric properties, they require higher *Q*-by-frequency ($Q×f$) and τ_f values closer to zero to satisfy the requirements of 5G/6G wireless technologies. Nonstoichiometry can lead to lattice distortion and defects. In addition, the sintering characteristics of ceramics can be improved

---

✉ Corresponding authors.
E-mail: K. Song, kxsong@hdu.edu.cn;
X. Li, lx100527@163.com;
H. Zhou, zhouhuanfu@163.com

by changing the stoichiometric ratio of the constituent elements [22–26]. Singh *et al.* [27] studied the effect of nonstoichiometric vanadium-ion ratios on the phase composition, microstructure, and Q value of $Ca_5Mn_4V_{6+x}O_{24}$ ($-0.15 \le x \le 0.05$), which is a microwave dielectric ceramic; A slight increase or decrease in vanadium-ion content did not influence the crystal structure. The $Ca_5Mn_4V_{5.9}O_{24}$ ceramic exhibited the best performance at $x = -0.1$, with a $Q\times f$ value of 39,141 GHz that significantly exceeded that of the $Ca_5Mn_4V_6O_{24}$ ceramic (33,800 GHz). Liu *et al.* [28] by preparing non-stoichiometric $Li_{(1+0.06)2}MgTi_3O_8$ ceramics to control the structure, showed the best dielectric properties, $Q\times f$ increased by 54% compared with $Li_2MgTi_3O_8$. Zhou *et al.* [29] prepared nonstoichiometric $Y_{3+x}Al_5O_{12}$ ($-0.12 \le x \le 0.12$) ceramics. This result confirms the excellent solubility of Y-rich compounds in YAG crystal structure and obtains excellent microwave dielectric properties: $\varepsilon_r = 11.18$, $Q\times f = 236{,}936$ GHz, and $\tau_f = -35.9$ ppm/℃. Pei *et al.* [30] prepared non-stoichiometric $Li_3Mg_2Sb_{1-x}O_6$ ($0.05 \le x \le 0.125$) compounds. The appropriate Sb deficiency in $Li_3Mg_2SbO_6$ not only does not affect the phase composition of the material but also reduces its sintering temperature and significantly improves its $Q\times f$ value.

In this study, we investigated the effects of nonstoichiometric Sr^{2+} ratios on the crystal phase structure, microstructure, and microwave dielectric properties of the SrY_2O_4 ceramic. In addition, the τ_f value of the $Sr_{1.02}Y_2O_{4.02}$ sample was adjusted by adding various amounts of $CaTiO_3$ (which has a large positive τ_f) to deliver a near-zero τ_f value. Finally, the temperature stability of a dielectric resonator antenna prepared using the $Sr_{1.02}Y_2O_{4.02}$+2wt% $CaTiO_3$ ceramic was evaluated.

2 Experimental

Ceramic $Sr_{1+x}Y_2O_{4+x}$ (x = 0–0.04) samples were prepared from high-purity $SrCO_3$ and Y_2O_3 powders (≥ 99%, Sinoarm Chemical Reagent Co., Ltd., Shanghai, China) using conventional solid-state chemistry. Hygroscopic Y_2O_3 was preheated at 900 ℃ for 2 h to remove moisture and then weighed. The powders were weighed, mixed according to the required composition, and ball-milled in ethanol using zirconia balls for 6 h. Each mixture was then dried at 90 ℃ in a drying oven and calcined at 1400 ℃ in air for 4 h. Then the calcined powder was ball-milled for 4 h under the same medium conditions and dried. A polyvinyl alcohol solution (5%) was added, and each sample was pressed into a 10-mm-diameter, 5-mm-thick cylinder. Samples were heated in air at 550 ℃ for 4 h to discharge their adhesives, after which they were sintered for 6 h in the temperature range of 1425–1525 ℃ at 5 ℃/min.

The phase structure of each sample was analyzed by the X-ray powder diffractometer (XRD; X'Pert PRO type, PANalytical, Almelo, the Netherlands). Rietveld refinement of the data was performed using GSAS software to calculate the relative phase content of each sample. The surface morphology of each sample was examined by the scanning electron microscope (SEM; JSM6380-LV, JEOL, Tokyo, Japan). Samples were subjected to high-resolution transmission electron microscopy (HRTEM), selected-area electron diffraction (SAED), and energy-dispersive X-ray spectroscopy (EDS) on transmission electron microscopes (TEM, JEM-2100F, JEOL, Japan) The elemental composition of each sample was determined by the X-ray photoelectron spectroscopy (XPS; ESCALAB 250Xi, Thermo Electron Corporation, USA). Before analysis, all samples were polished with 800-mesh sandpaper for 15 min and thermally etched at 1425 ℃ for 30 min. The ε_r and $Q\times f$ values of each sample were determined at microwave frequencies (300 kHz–20 GHz) using a network analyzer (E5071C, Agilent, Santa Clara, CA, USA). Resonant frequency changes in TE01δ mode were recorded, and τ_f values were calculated as Eq. (1):

$$\tau_f = \frac{f_T - f_0}{f_0\,(T - T_0)} \tag{1}$$

where f_0 and f_T are the resonant frequencies of the ceramic sample at T_0 = 25 ℃ and T = 85 ℃, respectively.

The relative density of each sample was calculated as Eq. (2):

$$\rho_r = \frac{\rho_m}{\rho_{th}} \times 100\% \tag{2}$$

where ρ_r, ρ_m, and ρ_{th} are the relative, bulk, and theoretical densities of the ceramic, respectively. Bulk densities were determined using the Archimedes method.

The dielectric resonator antenna was simulated using HFSS software. The proposed antenna consisted mainly of a dielectric substrate, a rectangular dielectric resonator fabricated using $Sr_{1.02}Y_2O_{4.02}$+2wt%$CaTiO_3$, and a SubMiniature version A connector; the antenna was excited by aperture coupling and showed excellent radiation characteristics. The rectangular dielectric resonator of the antenna was prepared by grinding the cylindrical sample into a rectangle. Adhesive tape was used to fix the dielectric resonator to the ground plane. The Keysight N5234B analyzer supports a frequency between 10 MHz and 43.5 GHz.

3 Results and discussion

The XRD patterns for the $Sr_{1+x}Y_2O_{4+x}$ (x = 0–0.4) ceramics sintered at 1475 ℃ for 6 h are shown in Fig. 1. The observed peaks were indexed to SrY_2O_4 (PDF#96-200-2283), which revealed that each $Sr_{1+x}Y_2O_{4+x}$ sample had the same phase structure as the SrY_2O_4 ceramic, namely, an orthorhombic crystal structure that belongs to the *Pnma*/62 space group. The absence of new peaks resulting from excess Sr is ascribable to several factors. First, excess Sr may form a solid solution with the matrix; in this case, no second phase is formed, leading to an unchanged crystal structure. Second, no new diffraction peaks are observed if a second phase is formed in only minimal amounts or is weakly reflective.

The internal structure of a crystal, including lattice type, atom

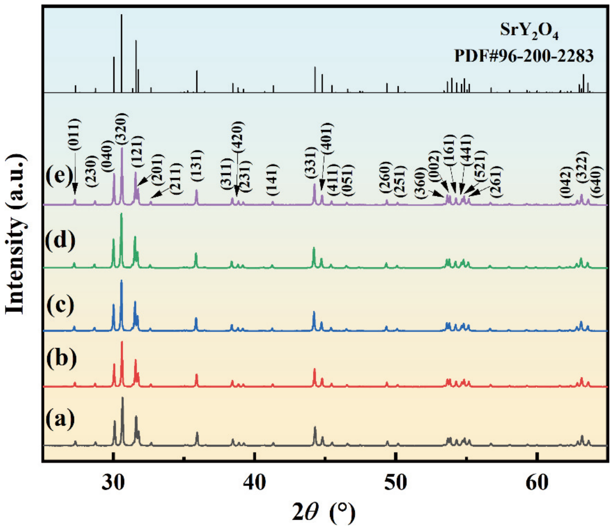

Fig. 1 XRD patterns of SrY_2O_4 (PDF#96-200-2283) and $Sr_{1+x}Y_2O_{4+x}$ samples sintered at 1475 ℃ for 6 h: (a) x = 0, (b) x = 0.01, (c) x = 0.02, (d) x = 0.03, and (e) x = 0.04.

type, atomic number, spatial position, network index, and diffraction index, determines the intensities of its diffraction peaks. The sample with $x = 0.02$ exhibited the strongest diffraction peaks, which indicated that $Sr_{1.02}Y_2O_{4.02}$ favored the growth of ordered crystal planes that led to the optimal degree of crystallization. In addition, the diffraction peaks initially shifted toward lower angles and then toward higher ones with increasing x. The Bragg equation ($2d\sin\theta = n\lambda$, where d is the interplanar spacing, θ is the diffraction angle, n is the number of diffraction orders, and λ is the wavelength of the incident light) reveals that the crystallographic spacing first increases and then decreases with increasing Sr content, as the wavelength does not change. The initial increase in θ is possibly due to the formation of solid solutions containing suitable amounts of Sr. Excess Sr possibly forms a high-melting SrO phase when the solid-solution limit is exceeded, hindering grain growth. Increasing the SrO-phase content decreases the intergrain spacing; consequently, the diffraction peaks shift to higher angles. This notion is further supported by SEM and EDS.

The XRD patterns of the ceramic samples were Rietveld-refined to provide structural details (Fig. 2). Lag and smoothing effects were observed at a fast scan rate of 0.417 s^{-1}, leading to defects such as diffraction-peak displacement, inferior resolution, and linear distortion. To avoid these issues, XRD data collected at a slower scan rate were Rietveld-refined, with results for the $Sr_{1.02}Y_2O_{4.02}$ sample sintered at 1475 ℃, which exhibited the best combination of microwave dielectric properties (Fig. 2(a)), with refined data listed in Table 1. Goodness-of-fit (GOF) and reliability factor (w_R) values of 4.62 and 9.949 were calculated, respectively, along with the following refined cell data: $\alpha = \gamma = \beta = 90°$, a = 10.07662 Å, b = 11.91356 Å, c = 3.40805 Å, and V = 409.131 $Å^3$. The calculated and measured data are similar, indicating that the results are reliable.

Figure 3 shows a structural diagram of SrY_2O_4 created using VESTA software. The structure of the SrY_2O_4 ceramic is similar to that of $CaFe_2O_4$, which belongs to the orthorhombic system and the *Pnma* space group. The structure of SrY_2O_4 contains Y atoms surrounded by six oxygen atoms, with the Sr atom surrounded by eight oxygen atoms; therefore, the Y and Sr atoms are six- and eight-coordinated, respectively. These coordination numbers were used to calculate the packing fraction of each sample (Fig. 9). The octahedral structure of the ceramic is composed of a Y_2O_{2-4} skeleton, in which Y atoms occupy two different sites; Y1 occupies an undeformed octahedral position, whereas Y2 occupies a distorted octahedral position because the Y^{3+} and O^{2-} ions have different radii. Sr is also located within this framework [17,21,32–35]. After determining the physical phases and crystal structures of $Sr_{1+x}Y_2O_{4+x}$ (x = 0.01–0.04), these ceramics were analyzed further in detail. Information regarding the SrY_2O_4 ceramic is provided in our previous study [31].

Generally, τ_f is believed to be related to the linear expansion coefficient (α_L) and the temperature coefficient of the dielectric constant (τ_ε) [36,37] as Eq. (3):

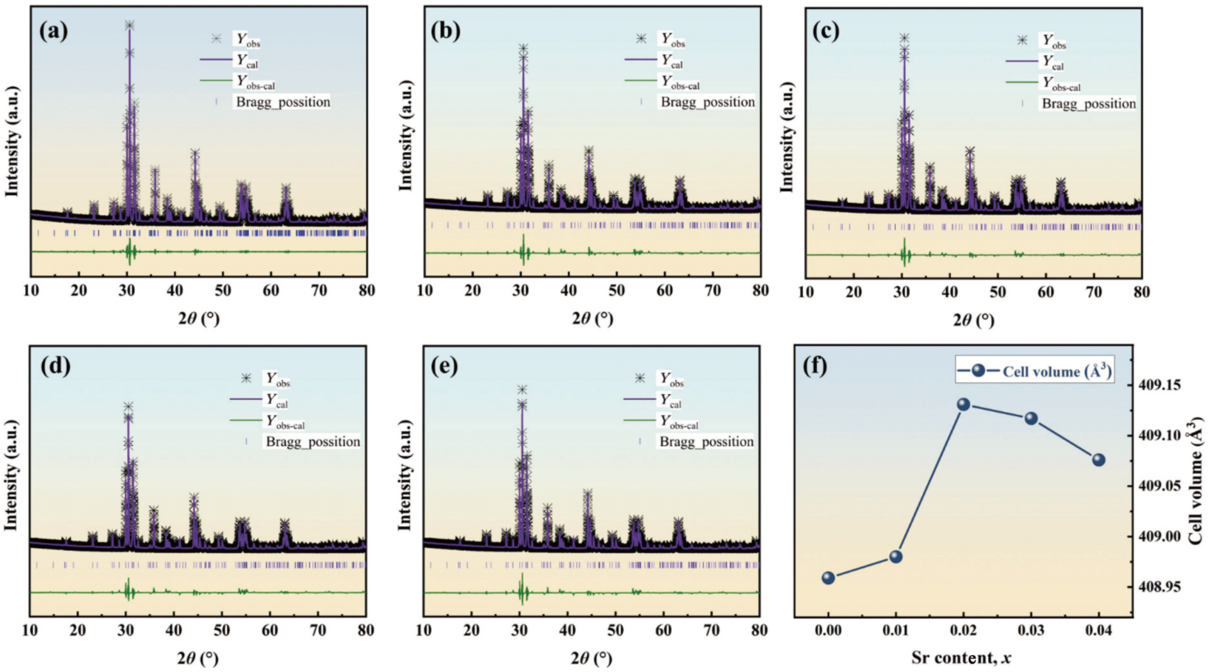

Fig. 2 XRD refinements for various $Sr_{1+x}Y_2O_{4+x}$ samples: (a) $x = 0$, (b) $x = 0.01$, (c) $x = 0.02$, (d) $x = 0.03$, and (e) $x = 0.04$. (f) Cell volume as a function of Sr content.

Table 1 Structural characteristics of $Sr_{1+x}Y_2O_{4+x}$ (x = 0–0.04) ceramics sintered at 1475 ℃ for 6 h

x	Reliability factor		Lattice parameter			V_{unit} ($Å^3$)	Ref.
			$\alpha = \beta = \gamma = 90°$				
	w_R	GOF	a (Å)	b (Å)	c (Å)		
0			10.07580	11.91180	3.40740	408.959	[31]
0.1	9.006	4.16	10.07580	11.91184	3.40755	408.980	This work
0.2	9.949	4.62	10.07662	11.91356	3.40805	409.131	This work
0.3	9.342	4.20	10.07635	11.91355	3.40802	409.117	This work
0.4	9.684	4.47	10.07594	11.91328	3.40790	409.076	This work

$$\tau_f = -\alpha_\mathrm{L} - \frac{\tau_\varepsilon}{2} \tag{3}$$

where τ_f is greatly influenced by τ_ε as α_L is typically −10 ppm/℃, and τ_ε is derived using the Clausius–Mossotti equation at constant pressure [36]:

$$\tau_\varepsilon = \left[\left(\frac{\partial V_m}{\partial T}\right)_P \frac{1}{3V_m} + \left(\frac{\partial \alpha_D}{\partial V_m}\right)_T \left(\frac{\partial V_m}{\partial T}\right)_P \frac{1}{3\alpha_D} + \left(\frac{\partial \alpha_D}{\partial T}\right)_{V_m} \frac{1}{3\alpha_D}\right] \times \left(\frac{\varepsilon_\mathrm{r}-2}{\varepsilon_\mathrm{r}+1}\right) \tag{4}$$

where α_D and V_m are the polarizability and volume of the sphere, respectively. The first two terms of this equation, which are related to volume expansion, offset each other and consequently have almost no effect on τ_ε. The third term represents the restoring force acting on the ion, which is inversely proportional to ion polarizability; hence, τ_f can be rationalized in terms of the structural parameters. The dielectric loss and temperature stability of a ceramic is closely related to its crystal structure. The ion order and oxygen octahedral tilt (octahedral distortion) are the main structural characteristics that affect the microwave dielectric properties of a material [37,38]. In this study, we used octahedral distortion to represent the structural evolution of SrY_2O_4. The degree of distortion associated with the $Y2O_6$ octahedron was calculated as Eq. (5):

$$\mathrm{Y2O_6\ distortion} = \frac{(\mathrm{Y-O})_\mathrm{largest} - (\mathrm{Y-O})_\mathrm{smallest}}{(\mathrm{Y-O})_\mathrm{average}} \times 100\% \tag{5}$$

where Y represents the yttrium atom and O represents the oxygen atom. The degrees of distortion for the $Y2O_6$ octahedra in ceramics with various Sr contents are listed in Table 2. Figure 4 shows that $Y2O_6$ distortion and the τ_f values exhibit similar trends; $Y2O_6$ distortion first decreases (from 8.5667% to 8.5643%) and then increases (to 8.5648%) with increasing Sr content. The τ_f value is negatively correlated with the recovery force between ions because a higher $Y2O_6$ distortion results in a weaker recovery force; therefore, τ_f gradually decreases with increasing temperature [31].

The grain size of each $Sr_{1+x}Y_2O_{4+x}$ sample (x = 0–0.04) sintered at 1475 ℃ for 6 h is shown in Figs. 5(a)–5(d), with corresponding SEM images shown in Figs. 5(e)–5(h). The surface morphology of the x = 0 sample has been described previously [31]. Grains first become smaller and then plateau in size as excess Sr is added. This behavior reveals that a small excess of Sr inhibits grain growth, most likely by forming a high-melting Sr-rich phase, such as SrO (melting point: 2430 ℃), at grain boundaries. Grains with uneven surfaces and varying sizes appear, including small grains (II) and

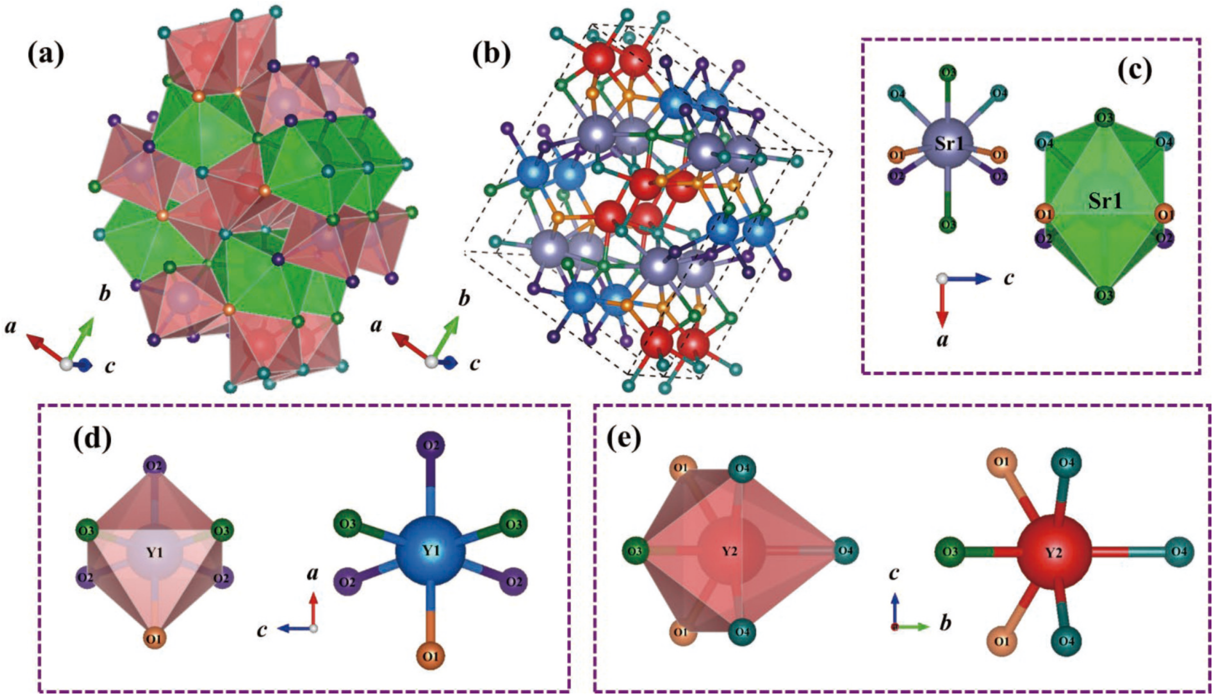

Fig. 3 (a, b) Crystal structure of SrY_2O_4, and coordination environment of different atoms: (c) Sr atom, (d) Y1 atom, and (e) Y2 atom .

Table 2 Bond lengths and distortion degrees of $Y2O_6$ octahedra at various Sr contents

x		0.01	0.02	0.03	0.04
Bond length (Å)	O4–Y2	2.37354 2.35649×2	2.37388 2.35676×2	2.37382 2.35663×2	2.37388 2.35672×2
	O1–Y2	2.40454×2	2.40483×2	2.40472×2	2.40480×2
	O3–Y2	2.20324	2.20353	2.20346	2.20352
	Max	2.40454	2.40483	2.40472	2.40480
	Min	2.20324	2.20353	2.20346	2.20352
	Average	2.34981	2.35010	2.35000	2.35007
Octahedral distortion (%)	$Y2O_6$	8.5667	8.5655	8.5643	8.5648

large grains (III), at high Sr excess (x = 0.04) (Fig. 5(h)). EDS point scanning was used to determine the phase compositions of grains (I), (II), and (III). Figures 5(i)–5(k) show that grain (I) is composed of 13.33, 28.24, and 58.43 at% Sr, Y, and O, respectively, which is similar to the 1:2:4 stoichiometry of the SrY_2O_4 ceramic. Significantly different proportions of Sr, Y, and O were observed in grain (II) (28.35, 0, and 71.65 at%, respectively), with grain (III) showing similar results. Hence, normally shaped grain (I) is composed of the SrY_2O_4 phase, whereas grains (II) and (III) are Y-free, having formed Sr-rich phases that coexist with the SrY_2O_4 phase.

We next examined the ceramic with the best combination of microwave dielectric properties (x = 0.02) using SEM, EDS, HRTEM, and SAED techniques to further investigate its crystal structure and phase composition. No encircling or complementary distribution features were observed in the EDS images (Figs. 6(b)–6(d)), which indicates that Sr, Y, and O are uniformly distributed in the sample and that no impurity phases had been generated. The blue dashed box in Fig. 6(a) highlights the sample region subjected to HRTEM; the image acquired along the [001] axis at room temperature (Fig. 6(e)) shows a perfectly arranged lattice. The indicated region in Figs. 6(f)–6(g) was subjected to fast Fourier transform (FFT) and inverse FFT analyses to produce an electron diffraction image in inverse space from which the crystallographic surface spacing was determined. Ten vertical crystallographic planes were examined to avoid random errors; the calculated crystal-plane spacing (5.274 Å) corresponds well to the (200) crystal plane of SrY_2O_4. Figure 6(i) shows the SAED pattern of the sample acquired along the [010] axis; the clear, sharp diffraction points indicate the formation of a calcium-iron oxide structure that belongs to the *Pnam* space group. These results confirm that the $Sr_{1.02}Y_2O_{4.02}$ ceramic prepared using solid-phase chemistry has an excellent crystal structure and is highly crystalline, which rationalizes its superior microwave dielectric properties.

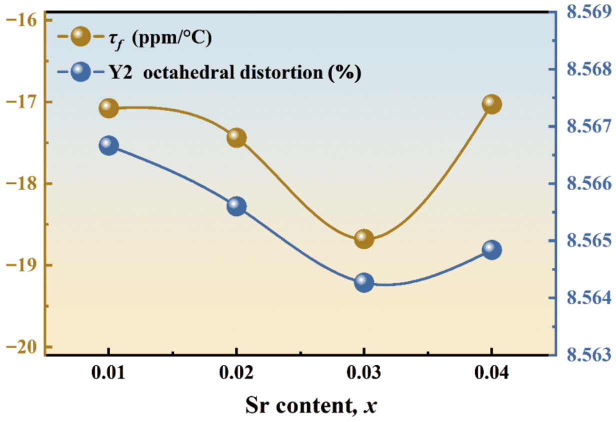

Fig. 4 Y2O_6 distortion and τ_f values for $Sr_{1+x}Y_2O_{4+x}$ (x = 0.01–0.04) ceramics as functions of Sr content.

Figure 7 shows Raman spectra of the $Sr_{1+x}Y_2O_{4+x}$ (x = 0–0.4) samples sintered at the optimized temperature. Figure 7(a) displays Raman peaks at 104, 219, 419, and 483 cm^{-1} corresponding to Y–O antisymmetric bending, O–Y–O antisymmetric stretching, Y–O symmetric bending, and O–Y–O symmetric stretching vibrations, respectively [39]. Specifically, $Sr_{1.02}Y_2O_{4.02}$ exhibits highly intense characteristic peaks at 77, 1193 and 1469 cm^{-1}. As the x value increases, the intensity of the characteristic peaks at 1193 and 1469 cm^{-1} gradually decreases, and the corresponding FWHM values gradually increase. Although the vibrational modes of these peaks are not yet clear, their intensities are positively correlated with the $Q\times f$ values measured for $Sr_{1+x}Y_2O_{4+x}$ (x = 0–0.4) ceramic samples. Phonon interactions are well-known to consume large amounts of energy, which increases the intrinsic dielectric loss. The full width at half maximum (FWHM) of a Raman peak is inversely proportional to the phonon lifetime. The damping coefficient of the lattice vibration decreases as the bandgap narrows, interactions between phonons decrease, and the phonon lifetime increases, which leads to a decrease in intrinsic dielectric loss. Dielectric loss (tanδ) and the FWHM of a characteristic Raman peak are calculated using Eqs. (6) and (7):

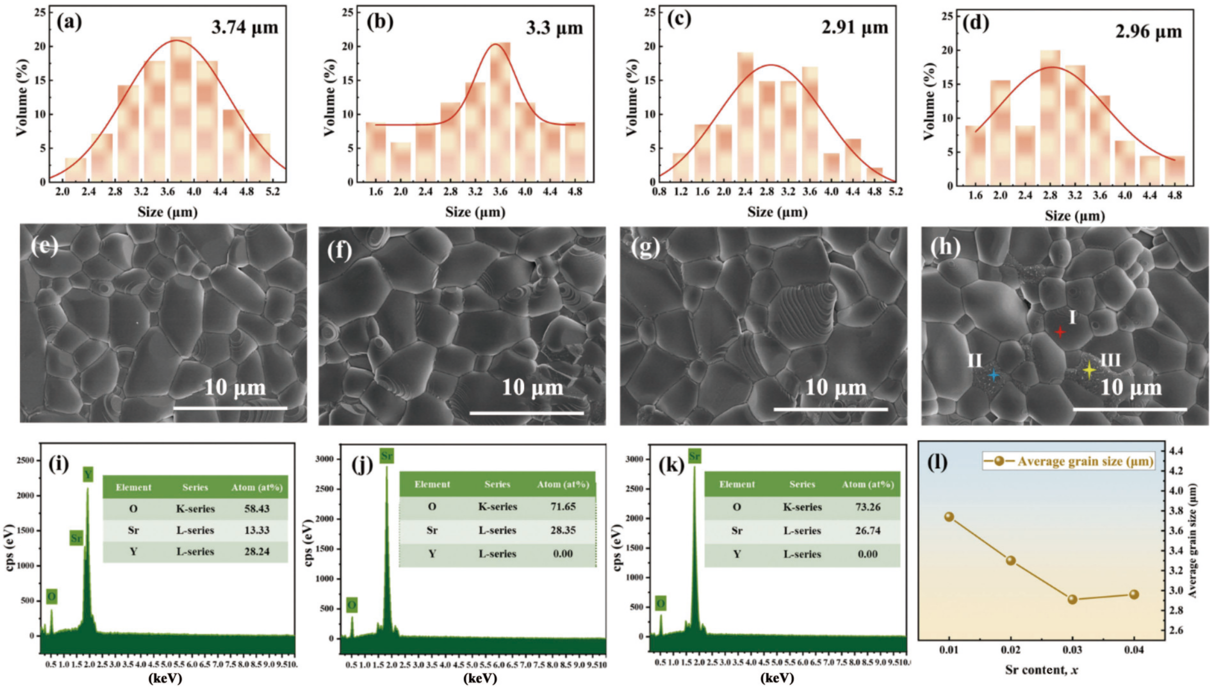

Element	Series	Atom (at%)
O	K-series	58.43
Sr	L-series	13.33
Y	L-series	28.24

Element	Series	Atom (at%)
O	K-series	71.65
Sr	L-series	28.35
Y	L-series	0.00

Element	Series	Atom (at%)
O	K-series	73.26
Sr	L-series	26.74
Y	L-series	0.00

Fig. 5 (a–d) Grain-size distributions and (e–h) SEM images of $Sr_{1+x}Y_2O_{4+x}$ ceramics sintered at 1475 ℃ for 6 h: (a, e) x = 0.01, (b, f) x = 0.02, (c, g) x = 0.03, and (d, h) x = 0.04. (i, k) EDS point scans of grains (I), (Ⅱ), and (Ⅲ) in panel (h), respectively. (l) Average grain size as a function of Sr content.

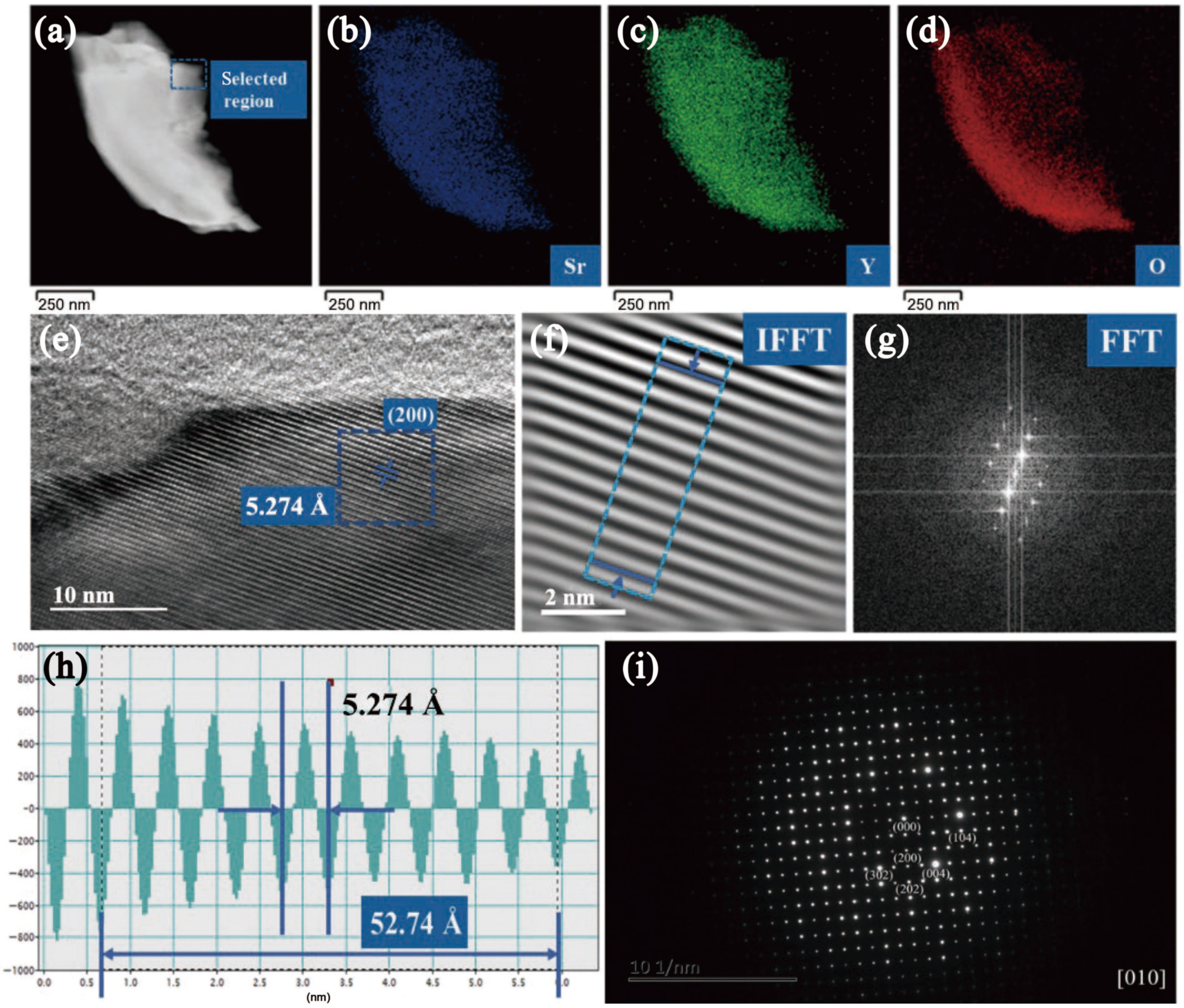

Fig. 6 (a–d) EDS spectra of $Sr_{1.02}Y_2O_{4.02}$ ceramic sample, (e) HRTEM image of $Sr_{1.02}Y_2O_{4.02}$ ceramic sample through [001] axis at room temperature, (f) IFFT image corresponding to the blue box region in (e), (g) FFT image corresponding to the blue box region in (e), (h) planar spacing image corresponding to the blue box region in (f), and (i) SAED image of $Sr_{1.02}Y_2O_{4.02}$ ceramic sample along [010] axis.

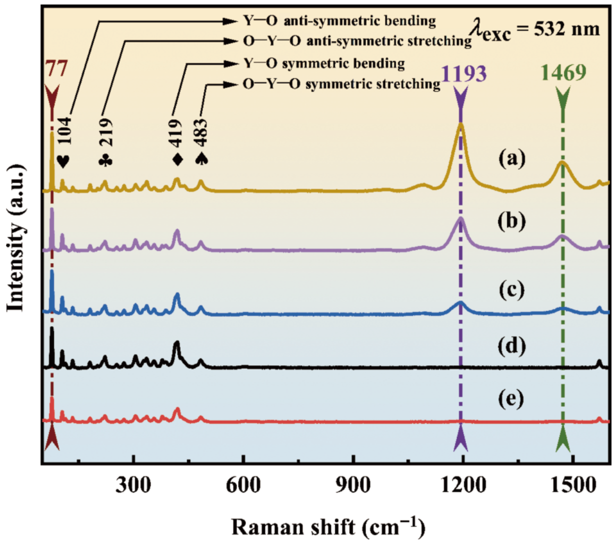

Fig. 7 Raman spectra of $Sr_{1+x}Y_2O_{4+x}$ samples at (a) $x = 0.02$, (b) $x = 0.03$, (c) $x = 0.01$, and (d) $x = 0.04$.

$$\tan\delta = \frac{\gamma\omega_0}{\omega_T^2} \tag{6}$$

$$\mathrm{FWHM} = \frac{\gamma\sqrt{\gamma^2 + 4\omega^2}}{2\omega_0} \tag{7}$$

where γ, ω_0, and ω_T denote the damping coefficient, central frequency of the optical mode, and angular frequency of the lattice vibration, respectively. Therefore, a smaller FWHM corresponds to a smaller intrinsic dielectric loss and a higher $Q \times f$ value [40]. In addition, the FWHM of diffraction peaks is closely related to sample crystallinity; a smaller FWHM corresponds to higher crystallinity, which leads to lower external losses caused by lattice defects and may be a reason for the higher $Q \times f$ values observed for microwave dielectric ceramics.

The microwave dielectric properties of a ceramic depend on internal factors (ionic polarizability and lattice vibration) as well as external factors (density and phase composition) [41,42]. Figure 8 shows that the relative dielectric constants of the $Sr_{1+x}Y_2O_{4+x}$ samples exhibit a similar trend to their relative densities. The $Sr_{1.02}Y_2O_{4.02}$ sample has a large relative density when sintered at 1475 ℃. We used Bosman and Havinga's correction [3] to eliminate the influence of porosity on the relative dielectric constant of each sample:

$$\varepsilon_{\mathrm{corrected}} = \varepsilon_{\mathrm{m}}(1 + 1.5p) \tag{8}$$

where $\varepsilon_{\mathrm{corrected}}$ and ε_{m} are the corrected and measured values of

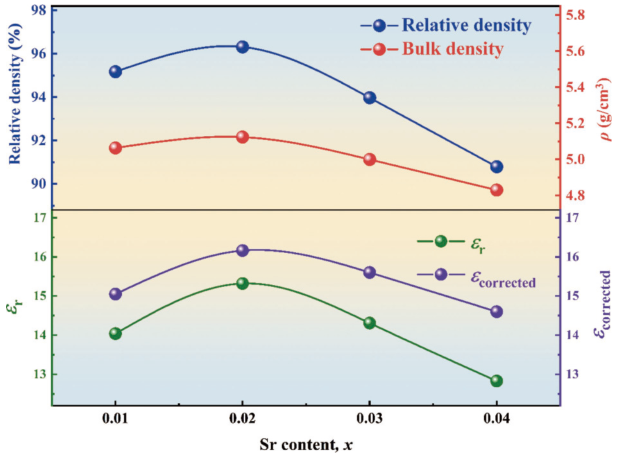

Fig. 8 Apparent density, relative density, ε_m, and $\varepsilon_{corrected}$ values of the $Sr_{1+x}Y_2O_{4+x}$ ceramics as functions of Sr content (x).

relative dielectric constant, respectively, and p is the porosity percentage. The amount of added Sr did not affect the $\varepsilon_{corrected}$ values of the $Sr_{1+x}Y_2O_{4+x}$ (x = 0–0.4) samples (which were slightly higher than the corresponding ε_m values) when the influence of porosity was excluded. This result reveals that porosity most critically affects the relative dielectric constant of the ceramic.

Theoretical relative dielectric constants (ε_{th}) were calculated using the Clausius–Mossotti equation [44]:

$$\varepsilon_{th} = \frac{3V_m + 8\pi\alpha}{3V_m - 4\pi\alpha} \tag{9}$$

where V_m is the molecular volume, and α is the polarizability of the SrY_2O_4. The total ionic polarizability of SrY_2O_4 was predicted using:

$$\alpha(SrY_2O_4) = \alpha\left(Sr^{2+}\right) + 2\alpha\left(Y^{3+}\right) + 4\alpha\left(O^{2-}\right) \tag{10}$$

where $\alpha(Sr^{2+})$, $\alpha(Y^{3+})$, and $\alpha(O^{2-})$ are the polarizabilities of Sr^{2+} (4.243 Å^3), Y^{3+} (3.813 Å^3), and O^{2-} (2.013 Å^3), respectively. These calculations reveal that SrY_2O_4 has a ε_{th} value of approximately 14.136, which is lower than its ε_m value, which is possibly ascribable to excess Sr.

Figure 9(a) shows $Q\times f$, packing fraction, bulk density, and FWHM of the 77 cm^{-1} Raman peak as functions of Sr content (x). The packing fraction is mainly used to describe cell-space utilization, which is often considered a major factor affecting the Q value of a microwave dielectric ceramic. Kim *et al.* [45] concluded that a higher packing fraction led to weaker vacancy scattering inside the crystal, which reduces loss in the system. Structural and atomic data were obtained for the samples through Rietveld refinement, from which packing fractions were calculated as Eq. (11):

$$\text{Packing fraction} = \frac{\frac{4\pi}{3}\times\left(r_{Sr}^3 + 2r_Y^3 + 4r_O^3\right)\times Z}{V} \tag{11}$$

where r_{Sr} (0.9 Å), r_Y (1.26 Å), and r_O (1.39 Å) are the effective ionic radii of Sr, Y, and O, respectively; V is the cell volume; Z = 4. A good Q factor is beneficial for selecting the band and enables more channels to be allocated to the same microwave band. Experimentally, Q is usually inversely proportional to frequency (f); consequently, $Q\times f$ is used to evaluate dielectric loss rather than only Q [46,47]. Figure 9(a) shows that the $Q\times f$ and stacking-fraction values of the ceramics in this study exhibit similar trends; both first increase and then decrease and show maximum values at x = 0.02. Hence, a change in the packing fraction leads to a corresponding change in $Q\times f$, in agreement with the conclusions of Kim *et al.* [45]. In addition to the packing fraction, the FWHM of the Raman peak is considered to be another intrinsic factor affecting the $Q\times f$ value of a ceramic, with a smaller FWHM leading to a higher $Q\times f$. As previously mentioned, three Raman peaks with unknown origins were observed in this study (77, 1193, and 1169 cm^{-1}). Using the Raman peak at 77 cm^{-1} as an example, Fig. 9(a) shows that the FWHM value first decreases and then increases with increasing Sr content, with the minimum value recorded at x = 0.02. Overall, FWHM is significantly negatively correlated with $Q\times f$, which is consistent with the observations of Cheng *et al.* [48]. Moreover, while bulk density is positively correlated with the dielectric constant in this study, it is positively correlated with $Q\times f$. This observation is easily understood in terms of the relationship between porosity and dielectric loss in a polycrystalline ceramic proposed by Penn *et al.* [49]:

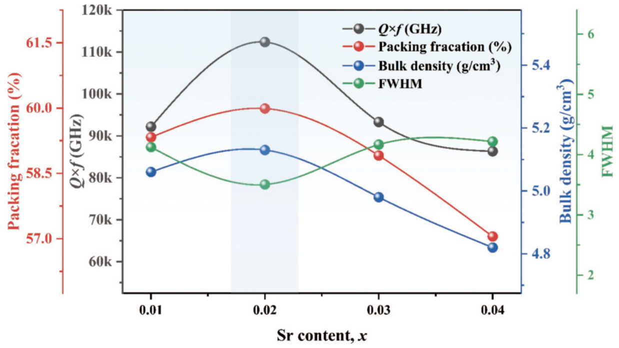

Fig. 9 $Q\times f$, FWHM, packing fraction, and bulk density of the $Sr_{1+x}Y_2O_{4+x}$ ceramics as functions of Sr content (x).

$$\tan\delta = (1-P)\tan\delta_0 + A'P\left(\frac{P}{1-P}\right)^{2/3} \tag{12}$$

where $\tan\delta$ is the experimentally measured dielectric loss, $\tan\delta_0$ is the loss in the ideal non-porous state, P is the porosity of the ceramic, and A' is a constant (9.277×10^{-3}). Therefore, a larger porosity is associated with a larger dielectric loss (i.e., a smaller Q (= $1/\tan\delta$)); the relationship between bulk density and $Q\times f$ in this study is well explained in terms of the negative correlation between porosity and bulk density. Figure 9(b) displays physical drawings of the samples of each component, which show that while samples are devoid of powdering, cracking, melting, and deformation at x = 0.01–0.03, cracking is observed at x = 0.04.

The τ_f value should be close to zero to meet the practical requirements of contemporary communications technologies. The τ_f value of the $Sr_{1.02}Y_2O_{4.02}$ sample was adjusted by adding various amounts of $CaTiO_3$ (1–4 wt%); Figs. 10(a)–10(c) reveal that how the added $CaTiO_3$ affects the ε_r, $Q\times f$, and τ_f values of the $Sr_{1.02}Y_2O_{4.02}$ ceramic sintered at 1500 ℃ for 6 h. The ε_r value was observed to increase from 15.79 to 17.98 with increasing $CaTiO_3$ content, which is ascribable to the relatively large dielectric constant of $CaTiO_3$ and is consistent with the superposition principle. The $Q\times f$ value decreased gradually as the amount of $CaTiO_3$ was increased to reach 24,463 GHz at 4 wt% $CaTiO_3$. These observations reveal that excessive $CaTiO_3$ results in a sharp decline in the performance of the $Sr_{1.02}Y_2O_{4.02}$ ceramic. The τ_f value was observed to gradually increase as the amount of dopant was increased because $CaTiO_3$ has a large positive τ_f value; a τ_f value of approximately 0 ppm/℃ was obtained at 2 wt% $CaTiO_3$. Overall, the $Sr_{1.02}Y_2O_{4.02}$ sample doped with 2 wt% $CaTiO_3$

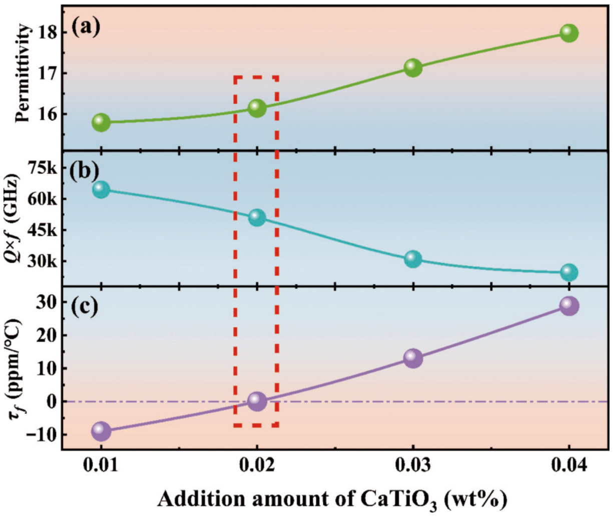

Fig. 10 (a) ε_r, (b) $Q\times f$, and (c) τ_f values of the $Sr_{1.02}Y_2O_{4.02}$ ceramic as functions of $CaTiO_3$ addition.

exhibited the best comprehensive microwave dielectric properties: $\varepsilon_r = 16.14$, $Q\times f = 51{,}004$ GHz, and $\tau_f \approx 0$ ppm/℃.

Table 3 lists various microwave dielectric ceramics with dielectric constants similar to those of the $Sr_{1+x}Y_2O_{4+x}$ (x = 0–0.04) ceramics in this study. Although $MnWO_4$ [50], $5MgO–Nb_2O_5–TiO_2$ [51], $YAlO_3$, $ErAlO_3$ [52], $ErNbO_4$ [53], $Nd_2Sn_2O_7$ [54], and $CaNb_2O_6$ [55] have relatively good dielectric properties that are similar to those of the $Sr_{1+x}Y_2O_{4+x}$ (x = 0–0.04) ceramics, their large τ_f values result in inferior temperature stability that limits their use in practical applications. On the other hand, while Ba_2SiO_4 [56], $Ca_4La_6(SiO_4)_4(VO_4)_2O_2$ [57], $Mg_3Nd_4Al_{44}O_{75}$ [58], $LaSrAlO_4$ [59], $BaO–0.35MgO–0.34WO_3–0.31TiO_2$, $BaO–0.33MgO–0.34WO_3–0.33TiO_2$ [60], and $SrPr_4Si_3O_{13}$ [61] have small τ_f values, their practical applications are limited by their low $Q\times f$ values. The $Sr_{1+x}Y_2O_{4+x}$ (x = 0–0.04) ceramics exhibited excellent microwave dielectric properties ($\varepsilon_r = 15.41$, $Q\times f$ = 112,375 GHz (at 8.99 GHz), and $\tau_f = -17.44$ ppm/℃) at x = 0.02. Moreover, the τ_f value of $Sr_{1.02}Y_2O_{4.02}$ was adjusted to almost zero by the addition of 2 wt% $CaTiO_3$ while maintaining good microwave dielectric properties ($\varepsilon_r = 16.14$, $Q\times f$ = 51,004 GHz, and $\tau_f = 0$ ppm/℃). In addition, the raw materials used to prepare the ceramic ($SrCO_3$ and Y_2O_3) and adjust the τ_f value ($CaCO_3$ and TiO_2) are readily available, which is a prerequisite for practical use in 5G/6G microwave communication devices.

Inspired by our results, we designed and fabricated a dielectric resonator antenna suitable for the millimeter band using the $Sr_{1.02}Y_2O_{4.02}$+2wt%$CaTiO_3$ ceramic. The configuration of the designed dielectric resonator antenna and its three-dimensional (3D) structure is shown in Fig. 11(a), with corresponding parameter values listed in Table 4, and photographic images shown in Figs. 11(b) and 11(c).

The 3D far-field gain image of the antenna at a central frequency of 26.6 GHz (Fig. 12(a)) shows that the electromagnetic signal most strongly radiates in the Z direction. Figures 12(b) and 12(c) show the cross-polarization (blue) and co-polarization (red) images in the E-plane and H-plane, respectively. Co-polarization in the E- and H-planes is more than 40 dB stronger than cross-polarization at $\theta = 0°$.

Figure 13(a) shows the simulated (black) and measured (red) S_{11} responses of the actual antenna. The simulated return loss was determined to be −37.58 dB with a central frequency of 26.59 GHz, whereas the return loss and central frequency were −25.71 dB and 26.6 GHz, respectively. Thus, while the simulated and measured frequencies are well-matched, the measured return

Table 3 Microwave dielectric properties of $Sr_{1+x}Y_2O_{4+x}$ (x = 0–0.04) ceramics and other reported cordierites

Ceramic composition	Crystal structure	ε_r	$Q\times f$ (GHz)	τ_f (ppm/℃)	Ref.
$Sr_{1.04}Y_2O_{4.04}$	Orthorhombic *Pnam*	13.8	86,317	−17	This work
$Sr_{1.03}Y_2O_{4.03}$	Orthorhombic *Pnam*	14.2	93,293	−19	This work
$Sr_{1.01}Y_2O_{4.01}$	Orthorhombic *Pnam*	14.4	92,185	−17	This work
$MnWO_4$	Monoclinic *P2/c*	14.5	32,000	−64	[48]
Ba_2SiO_4	Orthorhombic *Pmcn*	14.5	17,900	−17	[56]
$Ca_4La_6(SiO_4)_4(VO_4)_2O_2$	Hexagonal apatite *P63/m*	14.5	22,000	−20	[57]
SrY_2O_4	Orthorhombic *Pnam*	14.8	84,090	−15	[38]
$5MgO–Nb_2O_5–TiO_2$	Mixture	15.0	59,000	−77	[49]
$Mg_3Nd_4Al_{44}O_{75}$	Magnetoplumbite	15.0	11,000	35	[58]
$LaSrAlO_4$	Tetragonal *I4/mmm*	15.3	32,820	−17	[59]
$BaO–0.35MgO–0.34WO_3–0.31TiO_2$	Perovskite hexagonal	15.4	77,000	−8	[60]
$Sr_{1.02}Y_2O_{4.02}$	Orthorhombic *Pnam*	15.4	112,375	−17	This work
$BaO–0.33MgO–0.34WO_3–0.33TiO_2$	Perovskite hexagonal	15.6	67,000	−10	[60]
$SrPr_4Si_3O_{13}$	Hexagonal apatite *P63/m*	15.6	12,200	−9	[61]
$YAlO_3$	Perovskite hexagonal *P63/mmc*	15.7	58,000	−59	[51]
$Sr_{1.02}Y_2O_{4.02}$+0.01$CaTiO_3$	Orthorhombic *Pnam*	15.8	64,505	−9	This work
$Sr_{1.02}Y_2O_{4.02}$+0.02$CaTiO_3$	Orthorhombic *Pnam*	16.1	51,004	0	This work
$ErAlO_3$	Perovskite orthorhombic *Pbnm*	16.3	44,200	−40	[51]
$ErNbO_4$	Monoclinic fergusonite	16.6	43,900	−64	[54]
$Nd_2Sn_2O_7$	Cubic	17.0	33,100	55	[55]
$Sr_{1.02}Y_2O_{4.02}$+0.03$CaTiO_3$	Orthorhombic *Pnam*	17.1	31,034	13	This work
$CaNb_2O_6$	Columbite *Pbcn*	17.3	49,600	−53	[56]
$Sr_{1.02}Y_2O_{4.02}$+0.04$CaTiO_3$	Orthorhombic *Pnam*	17.8	24,663	29	This work

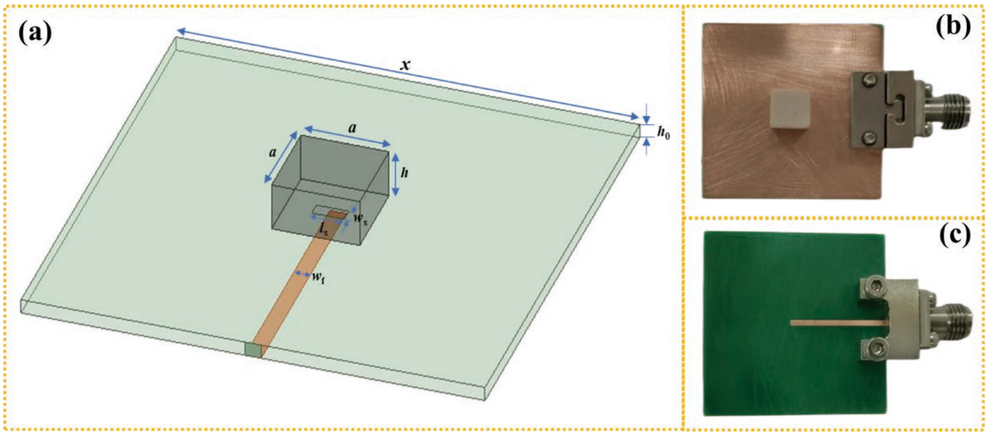

Fig. 11 (a) 3D structure of the antenna and its parameters. Photographic images of (b) top and (c) bottom of the antenna.

Table 4 Dielectric resonator antenna parameter values

(Unit: mm)

a	h	x	h_0	l_s	w_s	l_m	w_f
3.8	2	20	0.6	1.4	0.6	0.7	0.7

loss is slightly lower than the simulated value. Figure 13(b) shows the relationship between antenna input impedance and frequency for the real (black) and imaginary (red) parts of the input impedance. The *Z* value was determined to be 51.01+0.85i Ω at 26.6 GHz, which is close to 50 Ω. Figure 13(c) shows that the antenna has a voltage standing wave ratio (VSWR) of less than 2.0 in the 26–27 GHz frequency range and a minimum VSWR value of ~1.0 at the central frequency (26.6 GHz). A VSWR value close to unity indicates that the antenna is highly impedance-matched, with low power reflection and high radiated power. Figure 13(d) shows simulated antenna gain and efficiency data as frequency functions; gain and efficiency values of 3.66 dBi and 83.14%, respectively, were obtained at 26.6 GHz. Thus, the temperature-stabilized ($\tau_f = 0$) dielectric resonator antenna prepared using the $Sr_{1.02}Y_2O_{4.02}$+2wt%$CaTiO_3$ ceramic demonstrates good potential for use in the 5G millimeter-wave band (24.5–27.5 GHz) [62,63].

4 Conclusions

In this study, we used solid-phase chemistry to prepare $Sr_{1+x}Y_2O_{4+x}$ (x = 0–0.04) microwave dielectric ceramics and analyzed their sintering characteristics, phase structures, and microwave dielectric properties. $CaTiO_3$ was used to adjust the τ_f value of the ceramic, and the optimal sample with a near-zero τ_f value was used to prepare a dielectric resonator antenna. While XRD patterns of the $Sr_{1+x}Y_2O_{4+x}$ (x = 0–0.04) ceramics sintered at 1425–1525 ℃ match that of SrY_2O_4 (PDF#96-200-2283) well, their diffraction peaks first shifted to lower and then higher diffraction angles with increasing x. Rietveld refinement revealed that the cell volume of the ceramic tended to increase and then decrease with increasing x, which indicates that the cell volume is largely responsible for the observed diffraction-peak shifts. In addition, the τ_f value of the ceramic was found to be closely related to the distortion of its $Y2O_6$ octahedra and increased with increasing distortion. Furthermore, the $Q\times f$ value was determined to be proportional to the packing fraction and inversely proportional to the FWHM of the Raman peak. TEM revealed that the $Sr_{1.02}Y_2O_{4.02}$ sample has a good crystal structure and is highly crystalline. $Sr_{1.02}Y_2O_{4.02}$ was the densest ceramic prepared and exhibited the best microwave dielectric properties (ε_r = 15.41, $Q\times f$ = 112,375 GHz (at 8.99 GHz), and τ_f = −17.44 ppm/℃) among the $Sr_{1+x}Y_2O_{4+x}$ (x = 0–0.04) ceramics. In addition, the $Sr_{1.02}Y_2O_{4.02}$ sample doped with 2 wt% $CaTiO_3$ exhibited good integrated microwave dielectric properties (ε_r = 16.14, $Q\times f$ = 51,004 GHz, and τ_f = 0 ppm/℃); the values of these parameters changed in a manner consistent with the superposition principle when $CaTiO_3$ was added. Finally, a highly temperature-stable dielectric resonator antenna was prepared using the $Sr_{1.02}Y_2O_{4.02}$+2wt%$CaTiO_3$ ceramic. The antenna exhibited a central frequency of 26.6 GHz, with a gain and efficiency of 3.66 dBi and 83.14%, respectively, at this frequency, which highlights the good application potential of this antenna in the 5G millimeter-wave band (24.5–27.5 GHz).

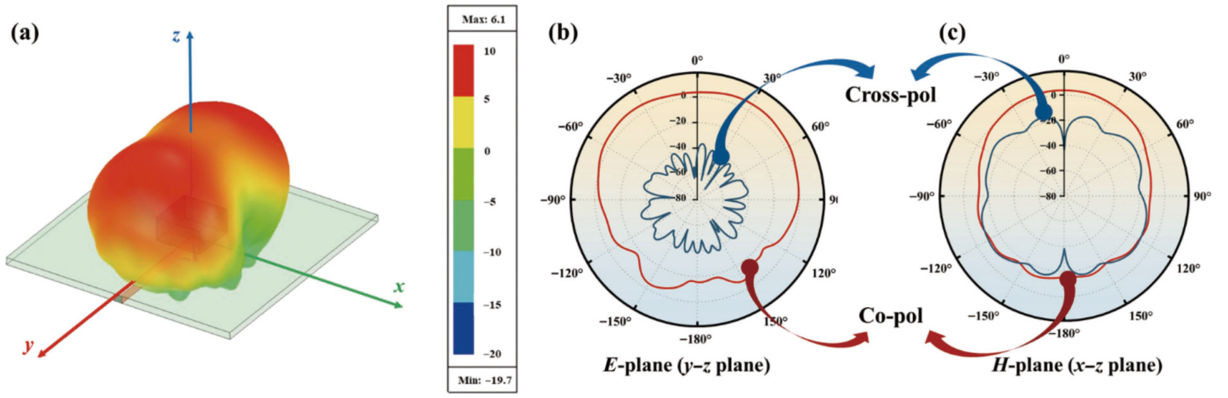

Fig. 12 (a) Simulated 3D radiation pattern at a resonant frequency of 26.6 GHz, and simulated co-polarization and cross-polarization images of (b) *E*- and (c) *H*-planes at a resonant frequency of 26.6 GHz.

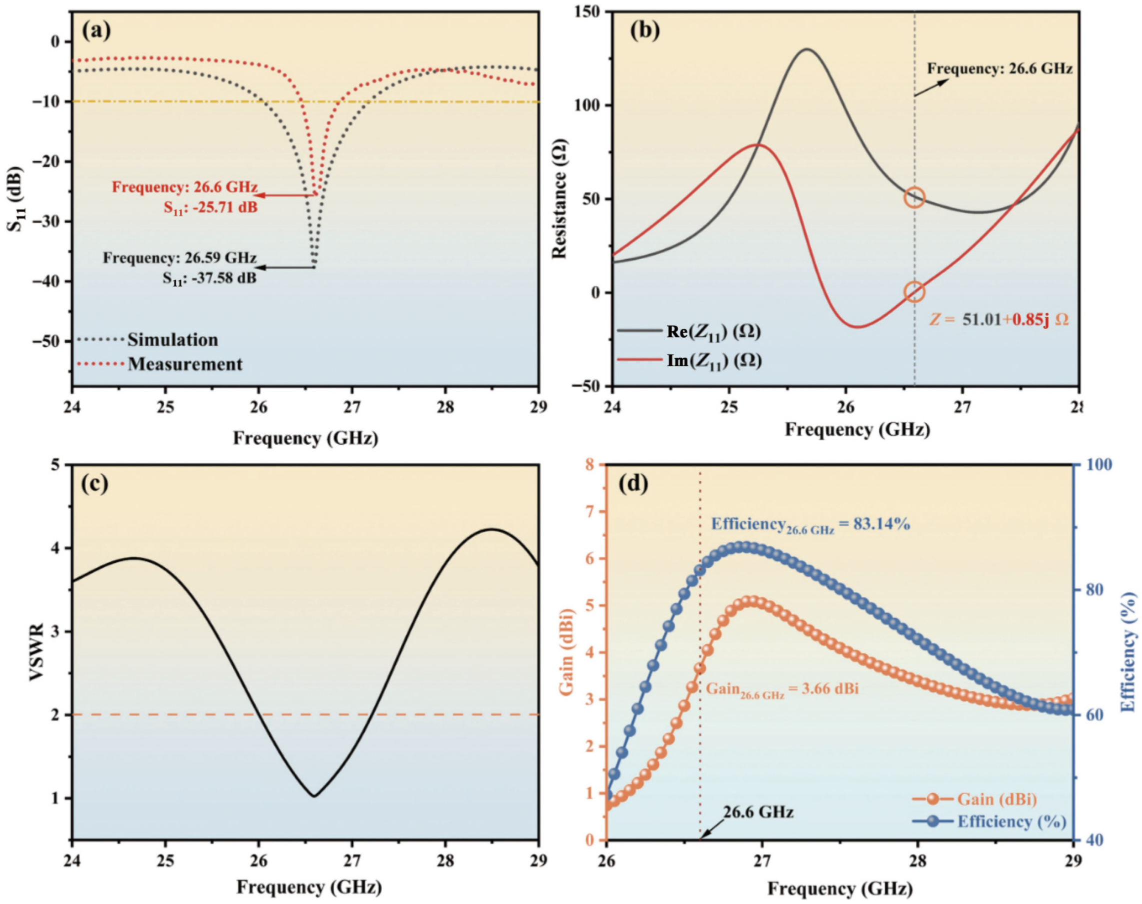

Fig. 13 (a) Simulated and measured S_{11} responses and (b) simulated Z parameters, (c) VSWRs, and (d) analog gains and efficiencies of the antenna.

Acknowledgements

This study was supported by the National Natural Science Foundation of China (Nos. 61761015 and 11664008), the Natural Science Foundation of Guangxi (No. 2018GXNSFFA050001), and the High Level Innovation Team and Outstanding Scholar Program of Guangxi Institutes.

Declaration of competing interest

The authors have no competing interests to declare that are relevant to the content of this article.

References

[1] Wang HQ, Li SX, Wang KG, *et al.* Sintering behaviour and microwave dielectric properties of MgO–2B$_2$O$_3$–x wt%BaCu(B$_2$O$_5$)–$y$wt%H$_3$BO$_3$ ceramics. *J Adv Ceram* 2021, **10**: 1282–1290.

[2] Chen DQ, Zhu XW, Xiong SY, *et al.* Tunable microwave dielectric properties in rare-earth niobates via a high-entropy configuration strategy to induce ferroelastic phase transition. *ACS Appl Mater Interfaces* 2023, **15**: 52776–52787.

[3] Liu YJ, He GQ, He YH, *et al.* Novel Sr$_3$Y$_2$Ge$_3$O$_{12}$ microwave ceramics: Sintering behavior, phase composition, microstructure and dielectric properties. *Ceram Int* 2023, **49**: 13150–13157.

[4] Feng C, Zhou X, Tao BJ, *et al.* Crystal structure and enhanced microwave dielectric properties of the Ce$_2$[Zr$_{1-x}$(Al$_{1/2}$Ta$_{1/2}$)$_x$]$_3$(MoO$_4$)$_9$ ceramics at microwave frequency. *J Adv Ceram* 2022, **11**: 392–402.

[5] Guo WJ, Ma ZY, Luo Y, *et al.* Structure, defects, and microwave dielectric properties of Al-doped and Al/Nd co-doped Ba$_4$Nd$_{9.33}$Ti$_{18}$O$_{54}$ ceramics. *J Adv Ceram* 2022, **11**: 629–640.

[6] He GQ, Liu YJ, He YH, *et al.* Sintering behavior, phase composition, microstructure and dielectric properties of SrSm$_2$O$_4$ microwave ceramics. *J Alloys Compd* 2022, **924**: 166475.

[7] Huang FY, Su H, Li YX, *et al.* Low-temperature sintering and microwave dielectric properties of CaMg$_{1-x}$Li$_{2x}$Si$_2$O$_6$ (x = 0–0.3) ceramics. *J Adv Ceram* 2020, **9**: 471–480.

[8] Peng R, Li YX, Su H, *et al.* Three-phase borate solid solution with low sintering temperature, high-quality factor, and low dielectric constant. *J Am Ceram Soc* 2021, **104**: 3303–3315.

[9] He GQ, Liu YJ, Zhou HF, *et al.* Sintering behavior, phase composition, microstructure, and dielectric characteristics of garnet-type Ca$_3$Fe$_2$Ge$_3$O$_{12}$ microwave ceramics. *J Materiomics* 2023, **9**: 472–481.

[10] Zhou MK, Tang B, Xiong Z, *et al.* Effects of MgO doping on microwave dielectric properties of yttrium aluminum garnet ceramics. *J Alloys Compd* 2021, **858**: 158139.

[11] He GQ, Wang HQ, Li Q, *et al.* A microwave dielectric ceramic with ultra-low dielectric constant prepared by reaction sintering method. *J Electron Mater* 2022, **51**: 5026–5031.

[12] Zhou X, Liu LT, Sun JJ, *et al.* Effects of (Mg$_{1/3}$Sb$_{2/3}$)$^{4+}$ substitution on the structure and microwave dielectric properties of Ce$_2$Zr$_3$(MoO$_4$)$_9$ ceramics. *J Adv Ceram* 2021, **10**: 778–789.

[13] He GQ, He YH, Liu YJ, *et al.* Sintering behaviour, phase composition, microstructure, and dielectric properties of BaSm$_2$O$_4$ microwave ceramics. *Ceram Int* 2023, **49**: 548–557.

[14] Fukushima H, Akatsuka M, Kimura H, *et al.* Optical and scintillation properties of Nd-doped strontium yttrate single crystals. *Sens Mater* 2021, **33**: 2235.

[15] Bouremani A, Kadri D, Kadari A, *et al.* Modeling of thermoluminescence in SrY$_2$O$_4$:Eu^{3+} and their concentration quenching effect. *Optik* 2021, **232**: 166607.

[16] Wang SX, Ma SW, Wu JM, *et al.* A promising temperature sensing strategy based on highly sensitive Pr^{3+}-doped SrRE$_2$O$_4$ (RE = Sc, Lu and Y) luminescent thermometers. *Chem Eng J* 2020, **393**: 124564.

[17] Gabbasov BF, Zverev DG, Gilmutdinov IF, *et al.* Spin-Hamiltonian parameters and zero-field splitting of impurity Gd^{3+} ions in SrY$_2$O$_4$ crystal. *J Magn Magn Mater* 2019, **469**: 638–642.

[18] Dubey V, Kaur J, Agrawal S, *et al.* Synthesis and characterization of Eu^{3+} doped SrY$_2$O$_4$ phosphor. *Optik* 2013, **124**: 5585–5587.

[19] Taikar DR. Synthesis and luminescence property of SrY_2O_4:M (M = Eu^{3+}, Tb^{3+}, Sm^{3+}, Ce^{3+}, Bi^{3+}) phosphors. *J Lumin* 2018, **204**: 24–29.

[20] Lojpur V, Stojadinovic S, Mitric M. Effect of Eu^{3+}-dopant concentration on structural and luminescence properties of SrY_2O_4 nanocrystalline phosphor and potential application in dye-sensitized solar cells. *Sci Sinter* 2018, **50**: 347–355.

[21] Wang YL, Chen XL, Su CX, *et al.* Phase transition and electric properties of $(1-x)BaTiO_3-xSr_{1.9}Ca_{0.1}NaNb_5O_{15}$ perovskite solid solutions. *J Mater Sci Mater Electron* 2013, **24**: 2873–2879.

[22] Fang L, Su CX, Wei ZH, *et al.* Phase structure, band gap and microwave dielectric properties of $Ba_8Ti_3Nb_{4-x}Sb_xO_{24}$ ceramics. *Ceram Int* 2013, **39**: 579–583.

[23] Xia W, Li LX, Ning P, *et al.* Relationship between bond ionicity, lattice energy, and microwave dielectric properties of $Zn(Ta_{1-x}Nb_x)_2O_6$ ceramics. *Ceram Int* 2013, **39**: 579–583.

[24] Reid DP, Stennett MC, Hyatt NC. The fluorite related modulated structures of the $Gd_2(Zr_{2-x}Ce_x)O_7$ solid solution: An analogue for Pu disposition. *J Solid State Chem* 2012, **191**: 2–9.

[25] Luan XW, Zhou HF, Zhang HL, *et al.* Enhancing the microwave dielectric performance of $SrSm_2Al_2O_7$ ceramic by Sr^{2+} nonstoichiometry and sintering aid addition. *J Eur Ceram Soc* 2020, **40**: 5494–5497.

[26] Li B, Qiu L, Tian JW. Enhanced effects of vanadium ions non-stoichiometry on the microstructure and microwave properties of $Ca_5Mn_4V_{6+x}O_{24}$ ceramics. *J Alloys Compd* 2018, **767**: 797–802.

[27] Singh V, Swapna K, Kaur S, *et al.* Narrow-band UVB-emitting Gd-doped SrY_2O_4 phosphors. *J Electron Mater* 2020, **49**: 3025–3030.

[28] Liu K, Liu C, Li J, *et al.* Relationship between structure and properties of microwave dielectric ceramic $Li_{(1+x)2}MgTi_3O_8$ based on Li nonstoichiometry. *J Materiomics* 2023, **9**: 279–288.

[29] Zhou M, Chen HT, Zhang X, *et al.* Phase composition, microstructure, and microwave dielectric properties of non-stoichiometric yttrium aluminum garnet ceramics. *J Eur Ceram Soc* 2022, **42**: 472–477

[30] Pei CJ, Tan JJ, Li Y, *et al.* Effect of Sb-site nonstoichiometry on the structure and microwave dielectric properties of $Li_3Mg_2Sb_{1-x}O_6$ ceramics. *J Adv Ceram* 2020, **9**: 588–594.

[31] He GQ, Ma XY, Liu YJ, *et al.* Sintering characteristics and microwave dielectric properties of ultralow-loss SrY_2O_4 ceramics. *Ceram Int* 2022, **48**: 21299–21304.

[32] Ghorpade SP, Kottam N, Melavanki R, *et al.* Photoluminescence, TGA/DSC and photocatalytic activity studies of Dy^{3+} doped SrY_2O_4 nanophosphors. *RSC Adv* 2020, **10**: 21049–21056.

[33] Priya R, Kaur S, Sharma U, *et al.* A review on recent progress in rare earth and transition metals activated SrY_2O_4 phosphors. *J Mater Sci Mater Electron* 2020, **31**: 13011–13027.

[34] Ghorpade SP, Hari Krishna R, Melavanki RM, *et al.* Effect of Eu^{3+} on optical and energy bandgap of SrY_2O_4 nanophosphors for FED applications. *Optik* 2020, **208**: 164533.

[35] Ramarao SD, Murthy VRK. Crystal structure refinement and microwave dielectric properties of new low dielectric loss $AZrNb_2O_8$ (A: Mn, Zn, Mg and Co) ceramics. *Scripta Mater* 2013, **69**: 274–277.

[36] Lai YM, Tang XL, Huang X, *et al.* Phase composition, crystal structure and microwave dielectric properties of $Mg_{2-x}Cu_xSiO_4$ ceramics. *J Eur Ceram Soc* 2018, **38**: 1508–1516.

[37] Wang S, Li LX, Wang XB. Low-temperature firing and microwave dielectric properties of $MgNb_{2-x}V_{x/2}O_{6-1.25x}$ ceramics. *Ceram Int* 2022, **48**: 199–204.

[38] Qin TY, Zhong CW, Shang Y, *et al.* Effects of LiF on crystal structure, cation distributions and microwave dielectric properties of $MgAl_2O_4$. *J Alloys Compd* 2021, **886**: 161278.

[39] Zhou D, Guo HH, Fu MS, *et al.* Anomalous dielectric behaviour during the monoclinic to tetragonal phase transition in $La(Nb_{0.9}V_{0.1})O_4$. *Inorg Chem Front* 2021, **8**: 156–163.

[40] Zhang Q, Su H, Zhong MF, *et al.* Bond characteristics and microwave dielectric properties on $Zn_{3-x}Cu_x(BO_3)_2$ ceramics with ultralow dielectric loss. *Ceram Int* 2021, **47**: 4466–4474.

[41] Lan XK, Li J, Zou ZY, *et al.* Lattice structure analysis and optimised microwave dielectric properties of $LiAl_{1-x}(Zn_{0.5}Si_{0.5})_xO_2$ solid solutions. *J Eur Ceram Soc* 2019, **39**: 2360–2364.

[42] Yin CZ, Yu ZZ, Shu LL, *et al.* A low-firing melilite ceramic $Ba_2CuGe_2O_7$ and compositional modulation on microwave dielectric properties through Mg substitution. *J Adv Ceram* 2021, **10**: 108–119.

[43] Roberts S. Polarizabilities of ions in perovskite-type crystals. *Phys Rev* 1951, **81**: 865–868.

[44] Zhou XJ, Wang KG, Hu S, *et al.* Preparation, structure and microwave dielectric properties of novel La_2MgGeO_6 ceramics with hexagonal structure and adjustment of its τ_f value. *Ceram Int* 2021, **47**: 7783–7789.

[45] Kim ES, Chun BS, Freer R, *et al.* Effects of packing fraction and bond valence on microwave dielectric properties of $A^{2+}B^{6+}O_4$ (A^{2+}: Ca, Pb, Ba; B^{6+}: Mo, W) ceramics. *J Eur Ceram Soc* 2010, **30**: 1731–1736.

[46] Wu SP, Chen DF, Jiang C, *et al.* Synthesis of monoclinic $CaSnSiO_5$ ceramics and their microwave dielectric properties. *Mater Lett* 2013, **91**: 239–241.

[47] Yoon SH, Kim DW, Cho SY, *et al.* Investigation of the relations between structure and microwave dielectric properties of divalent metal tungstate compounds. *J Eur Ceram Soc* 2006, **26**: 2051–2054.

[48] Cheng HF, Chia CT, Liu HL, *et al.* Spectroscopic characterization of $BA(MG_{1/3}TA_{2/3})O_3$ dielectrics for the application to microwave communication. *J Electromagn Waves Appl* 2007, **21**: 629–636.

[49] Penn SJ, Alford NM, Templeton A, *et al.* Effect of porosity and grain size on the microwave dielectric properties of sintered alumina. *J Am Ceram Soc* 1997, **80**: 1885–1888.

[50] Bijumon PV, Sebastian MT, Mohanan P. Experimental investigations and three-dimensional transmission line matrix simulation of $Ca_{5-x}A_xB_2TiO_{12}$ (A = Mg, Zn, Ni, and Co; B = Nb and Ta) ceramic resonators. *J Appl Phys* 2005, **98**: 124105.

[51] Cho SY, Kim IT, Hong KS. Microwave dielectric properties and applications of rare-earth aluminates. *J Mater Res* 1999, **14**: 114–119.

[52] Kim DW, Kwon DK, Yoon SH, *et al.* Microwave dielectric properties of rare-earth ortho-niobates with ferroelasticity. *J Am Ceram Soc* 2006, **89**: 3861–3864.

[53] Chen YC, Chen KC, Lee WC. Effect of sintering temperature and time on microwave dielectric properties of lanthanum tin oxide. *J Mater Sci Mater Electron* 2013, **24**: 1878–1882.

[54] Pullar RC, Breeze JD. Microwave dielectric properties of columbite-structure niobate ceramics, $M^{2+}Nb_2O_6$. *Key Eng Mater* 2002, **224–226**: 1–4.

[55] Joseph T, Sebastian MT. Microwave dielectric properties of alkaline earth orthosilicates M_2SiO_4 (M = Ba, Sr, Ca). *Mater Lett* 2011, **65**: 891–893.

[56] Thomas D, Abhilash P, Sebastian MT. Effect of isovalent substitutions on the microwave dielectric properties of $Ca_4La_6(SiO_4)_4(PO_4)_2O_2$ apatite. *J Alloys Compd* 2013, **546**: 72–76.

[57] Kagata H, Saito R, Katsumura H. Al_2O_3–MgO–ReO_x (Re: Rare earth)-based LTCC and its application to multilayer non-shrinkage substrate for microwave devices. *J Electroceram* 2004, **13**: 277–280.

[58] Liu XQ, Chen XM, Xiao Y. Preparation and characterization of $LaSrAlO_4$ microwave dielectric ceramics. *Mater Sci Eng B* 2003, **103**: 276–280.

[59] Takahashi H, Ayusawa K, Sakamoto N. Microwave dielectric properties of $Ba(Mg_{1/2}W_{1/2})O_3-BaTiO_3$ ceramics. *Jpn J Appl Phys* 1997, **36**: 5597.

[60] Thomas S, Sebastian MT. Microwave dielectric properties of $SrRE_4Si_3O_{13}$ (RE = La, Pr, Nd, Sm, Eu, Gd, Tb, Dy, Er, Tm, Yb, and Y) ceramics. *J Am Ceram Soc* 2009, **92**: 2975–2981.

[61] Jiang Y, Liu H, Muhammad R, *et al.* Broadband and high-efficiency of garnet-typed ceramic dielectric resonator antenna for 5G/6G communication application. *Ceram Int* 2022, **48**: 26922–26927.

[62] Wu FF, Zhou D, Du C, *et al.* Design of a sub-6 GHz dielectric resonator antenna with novel temperature-stabilized $(Sm_{1-x}Bi_x)NbO_4$ (x = 0–0.15) microwave dielectric ceramics. *ACS Appl Mater Interfaces* 2022, **14**: 7030–7038.

[63] Guo HH, Fu MS, Zhou D, *et al.* Design of a high-efficiency and-gain antenna using novel low-loss, temperature-stable $Li_2Ti_{1-x}(Cu_{1/3}Nb_{2/3})_xO_3$ microwave dielectric ceramics. *ACS Appl Mater Interfaces* 2021, **13**: 912–923.